ACS APPLIED MATERIALS & INTERFACES

Research Article

www.acsami.org

# Structural, Chemical, Optical, and Electrical Evolution of $SnO_x$ Films Deposited by Reactive rf Magnetron Sputtering

Hao Luo, Ling Yan Liang,* Hong Tao Cao,* Zhi Min Liu, and Fei Zhuge

Division of Functional Materials and Nano Devices, Ningbo Institute of Material Technology and Engineering, Chinese Academy of Sciences, Ningbo 315201, People's Republic of China

**ABSTRACT:** In this paper, $SnO_x$ films were produced by reactive radio frequency magnetron sputtering under various oxygen partial pressure ($P_O$) in conjunction with a thermal annealing at 200 °C afterwards. The obtained $SnO_x$ films were systematically studied by means of various techniques, including X-ray diffraction, Raman spectroscopy, X-ray photoelectron spectroscopy, spectroscopic ellipsometry, and Hall-effect measurement. The structural, chemical, and electrical evolution of the $SnO_x$ films was found to experience three stages: polycrystalline SnO phase dominated section with p-type conduction at $P_O \leq 9.9\%$; amorphous $SnO_2$ phase dominated area at $P_O \geq 12.3\%$, exhibiting n-type characteristics; and conductivity dilemma area in between the above mentioned sections, featuring the coexistence of SnO and $SnO_2$ phases with compatible and opposite contribution to the conductivity. The polycrystalline to amorphous film structure transition was ascribed to the enhanced crystallization temperature due to the perturbed structural disorder by incorporating $Sn^{4+}$ into the SnO matrix. The inversion from p-type to n-type conduction with $P_O$ variation is believed to result from the competition between the donor and acceptor generation process, i.e., the n-type behavior would be present if the donor effect is overwhelming, and vice versa. In addition, with increasing $P_O$, the refractive index decreased from 3.0 to 1.8 and the band gaps increased from 1.5 to 3.5 eV, respectively.

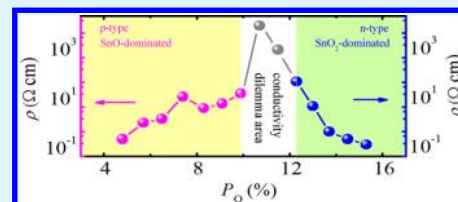


**KEYWORDS:** *$SnO_2$, SnO, reactive magnetron sputtering, XRD, XPS, Raman, ellipsometry, Hall effect*

## ■ INTRODUCTION

Stannic oxide ($SnO_2$), because of its excellent n-type semiconductor with low electrical resistance and high optical transparency in the visible range, is widely explored in various applications, such as transparent electrodes,[1] n-type thin film transistors (TFTs),[2] solar cells,[3] gas sensors,[4] etc. As another important tin oxide, stannous oxide (SnO) has also attracted ever-increasing attention for the applications as active layer in gas sensors,[5,6] as anode material for lithium rechargeable batteries,[7−9] and as a precursor for the production of $SnO_2$.[10] Especially, p-type TFTs have been fabricated by using SnO as p-channel material,[11−14] and ambipolar SnO TFTs have been demonstrated by controlling the channel thickness.[15] Very recently, we reported SnO-based ambipolar TFTs as well as ambipolar inverters, manifesting that the stoichiometry of the nominal SnO has a big impact on the ambipolar symmetry of the TFTs.[16]

Tin oxides ($SnO_x$) films can be prepared by various techniques, such as electron beam evaporation,[12] pulsed laser deposition,[13] chemical vapor deposition,[17] aqueous solution process,[18] hydrothermal synthesis,[19] magnetron sputtering,[11,20,21] etc., among which magnetron sputtering technique was utilized intensively. But whereas, most of research endeavors on tin oxides were mainly focused not on SnO, but on $SnO_2$ or foreign element dopped $SnO_2$. Muranaka et al.[20] and Beensh et al.[21] respectively produced $SnO_x$ films by magnetron sputtering using Sn metallic target at different oxygen partial pressure, and in particular, $\beta$-Sn and $\alpha$-SnO phases were obtained at low oxygen partial pressure. However, their main concerns were on the performance of $SnO_2$ films, without systematically studying on the physical properties of SnO. Recently, Fortunato et al.[11] prepared p-type $SnO_x$ films by reactive rf magnetron sputtering at different oxygen partial pressure for the usage of TFT channels, but a thorough investigation of the material's properties is still lacking.

In this study, $SnO_x$ films were fabricated by reactive rf magnetron sputtering through controlling the oxygen partial pressure, and the structural, chemical, optical, and electrical properties of the films were comprehensively investigated. The results can provide a robust addition to the knowledge base for the fabrication and the physical properties of $SnO_x$ films, which is indispensable whether for the fundamental research or the market-driven applications.

## ■ EXPERIMENTAL SECTION

A series of $SnO_x$ films were prepared on quartz glasses by reactive rf magnetron sputtering, applying a 2 in. Sn metallic target (99.99%) at a power of 60 W. Prior to deposition, the substrates were cleaned by organic solvents (alcohol and acetone), deionized $H_2O$, and subsequently dried in $N_2$ gas flow. After evacuating below $1 \times 10^{-4}$ Pa, $SnO_x$ films were deposited at room temperature through controlling the $O_2$ and Ar gas flux at a constant working pressure of 0.46 Pa. The oxygen partial pressure $P_O$ ($P_O = O_2/(O_2+Ar)\%$) varied from 4.8 to 15.3%. Films with a thickness in the range of 190−230 nm were obtained by fixing the deposition time for 30 minutes. The film

Received: August 9, 2012
Accepted: October 1, 2012
Published: October 1, 2012

ACS Publications © 2012 American Chemical Society

thickness increases monotonously with $P_O$ due to more $O_2$-induced weight and volume variation.[20] Finally, the as-deposited $SnO_x$ films were subjected to a thermal annealing at 200 °C for 2 h in air.

The phase composition of the films was characterized by X-ray diffraction (XRD, Bruker D8 Advance X-ray diffractometer) with Cu $K_\alpha$ radiation. The microstructure was elucidated by a confocal microscope Raman spectrometer (Renishaw inVia-Reflex) using a 532 nm excitation line which is created by second harmonic generation (SHG) element from a line of 1064 nm generated by Nd:YAG laser. The wavenumber is changed from 50 to 900 $cm^{-1}$ and the light-spot size is about 1 $\mu$m in diameter. The chemical composition was examined by X-ray photoelectron spectroscopy (XPS, Kratos Analytical Ltd., UK) using Al−$K_\alpha$ radiation. The optical properties were analyzed on a spectroscopic ellipsometry (SE, J.A. Woollam Inc.) in the range of 300−1700 nm. The electrical measurements were carried out at room temperature using a Hall-effect measurement system (HL5500).

## RESULTS AND DISCUSSION

**Phase and Microstructure Characteristics.** Figure 1 shows the XRD patterns of the $SnO_x$ films at various $P_O$. At $P_O$ = 4.8%, both $\alpha$-SnO phase ($\alpha$-PbO structure, P4/nmm, JCPDS card No.06-0395) and $\beta$-Sn phase ($I4_1$/amd, JCPDS card No.19-1365) were observed in the films, but the former one dominated. As $P_O$ increased, the intensity of $\beta$-Sn phase tapered and disappeared eventually at $P_O$ = 6.5%, in completely contrast to the variation trend of $\alpha$-SnO phase. As $P_O$ changed from 6.5 to 9.9%, only $\alpha$-SnO phase with more attenuated peak intensity was observed. When $P_O \geq$ 10.7%, there were no characteristic peaks for any phases perceived, suggesting the amorphous nature the films.

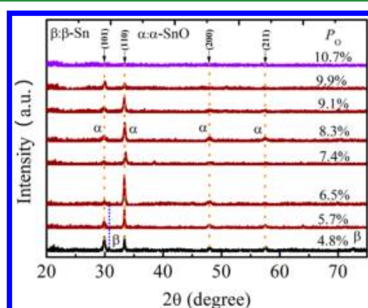


Figure 1. XRD patterns of the $SnO_x$ films deposited at different oxygen partial pressure ($P_O$).

Raman measurements were utilized to identify Raman active phonon modes of the films, as displayed in Figure 2. Only two peaks located at 112 and 210 $cm^{-1}$ which were indexed to the vibrational modes of SnO were observed for the polycrystalline $SnO_x$ films ($P_O \leq$ 9.9%), whereas no Raman-active mode (~42.4 and 126.6 $cm^{-1}$)[22−24] of $\beta$-Sn was present for the films even with the highest metallic Sn content ($P_O$ = 4.8%), which is probably related to the intensive light absorption caused by the metallic particles or/and clusters. Moreover, no $SnO_2$ characteristic peaks (~474, 632, 774 $cm^{-1}$)[25,26] were identified as well. $SnO_2$ phase, if presented and dominated at higher $P_O$ (≥10.7%), is still in the amorphous format, because 200 °C is too low to make $SnO_2$ crystallized (>400 °C).[27] As shown in Figure 2, the Raman characteristic peaks disappeared completely at $P_O \geq$ 10.7% as the polycrystalline films were converted into amorphous ones. As a result, it is reasonably believed that the phonon scattering volume related to $SnO_2$ in this case is under the observation threshold of the Raman equipment. The designation of the two observed characteristic peaks of SnO will be discussed in the following.

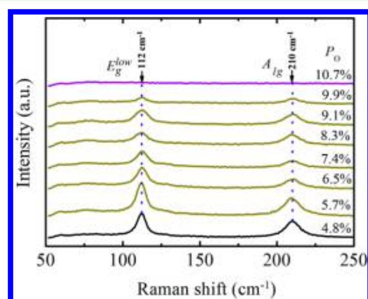


Figure 2. Raman spectra of the $SnO_x$ films fabricated at various oxygen partial pressure ($P_O$).

The vibrational modes of SnO described by the group theory can be expressed as follows:[28]

$$\Gamma = A_{1g} + B_{1g} + 2E_g + A_{2u} + E_u + 3 \text{ acoustic modes} \quad (1)$$

of which $A_{1g}$, $B_{1g}$, $E_g$ are Raman active, whereas $A_{2u}$, $E_u$ are infrared-related modes. Figure 3 manifests the atomic displacements of $A_{1g}$, $B_{1g}$, and $E_g$ modes. $A_{1g}$ mode is polarized in the z direction, in which Sn atoms are vibrating along z axis toward or away from the $x$−$y$ plane. $B_{1g}$ mode is also polarized in the $z$ direction, but the O atoms are vibrating out of the $x$−$y$ plane. By comparison, two $E_g$ modes, which are polarized within the $x$−$y$ plane, involve vibrations within each sublattice and of one sublattice with respect to the other, respectively.[24] The peak at 210 $cm^{-1}$ was assigned to $A_{1g}$ mode definitely, in line with the theoretical calculations and experimental reports.[24,28,29] However, there is a bifurcation on the identification of the peak at 112 $cm^{-1}$. Geurts et al. believed that this peak can be ascribed to the $B_{1g}$ mode.[28] The phonon frequency of $B_{1g}$ was calculated to be 370, 350, and 357 $cm^{-1}$ through ab initio full-potential linear-muffin-tin-orbital method, linear augmented-plane-wave calculation, and shell model, respectively.[24,29] Moreover, it is unreasonable that $B_{1g}$ has a frequency ($\omega$) lower than $A_{1g}$, considering that the mass ($m$) of O is smaller than Sn, because $B_{1g}$ and $A_{1g}$ modes are, respectively, O and Sn displacements, as the schematic illustrated in Figure 3 (in this case, $\omega \approx m^{-1/2}$).[24] In fact, the phonon frequency of $E_g^{low}$ ranges from 113 to 143 $cm^{-1}$ on the basis of the theoretical calculations. Thus, it is logically believed that the Raman peak at 112 $cm^{-1}$ should be allotted to the low frequency $E_g^{low}$ mode.

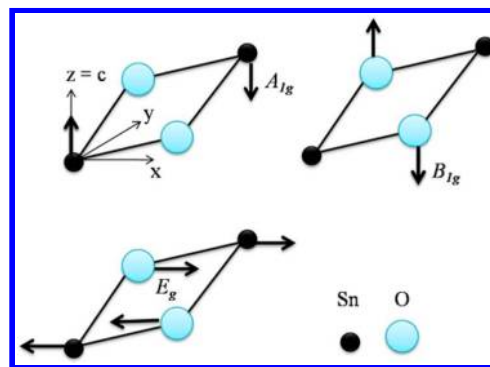


Figure 3. Schematic diagram to describe the atomic displacements of $A_{1g}$, $B_{1g}$, and $E_g$ vibrating modes.


dx.doi.org/10.1021/am301601s | ACS Appl. Mater. Interfaces 2012, 4, 5673−5677

**Chemical Composition Analysis.** XPS measurements were performed to further confirm the chemical composition of the films. High doses of argon ions (Ion energy of 2 KeV, current density of 5 $\mu A/cm^2$ roughly) were used to sputter away the outmost layer, to get rid of the carbon contamination as well as the hydrated layer so as to obtain the actual composition of the $SnO_x$ films. The binding energy data were calibrated with respect to the C1s signal of ambient hydrocarbons (C−H and C−C) at 284.8 eV.

Panels a and b in Figure 4 illustrate the typical core-level spectra of Sn 3d and O 1s, respectively. At $P_O$ = 4.8%, the Sn 3d spectrum depicts a spin-orbit doublet peak located at ~485.9 eV ($Sn^{2+}$ $3d_{5/2}$) and ~494.3 eV ($Sn^{2+}$ $3d_{3/2}$) with two shoulders centered at ~484.4 eV ($Sn^0$ $3d_{5/2}$) and ~492.8 eV ($Sn^0$ $3d_{3/2}$). As $P_O$ increased, the two shoulders gradually disappeared, whereas the chief peaks shifted to higher binding energies due to the presence of $Sn^{4+}$ (486.6 eV and 495.0 eV for $3d_{5/2}$ and $3d_{3/2}$, respectively). Along with continuously increasing $P_O$, the content of $Sn^{4+}$ became more and more, and gradually dominated at $P_O \geq 12.3\%$. Correspondingly, the evolution of O 1s spectra agrees well with that of Sn 3d spectra, as shown in Figure 4b. At $P_O$ = 4.8%, the O 1s spectrum only showed one peak at 529.8 eV assigned to O−$Sn^{2+}$. As $P_O$ increased, another peak centered at 530.4 eV (O−$Sn^{4+}$) presented and gradually became dominant. The binding energies of all the components in this experiment are consistent with the previously reported values.[30,31]

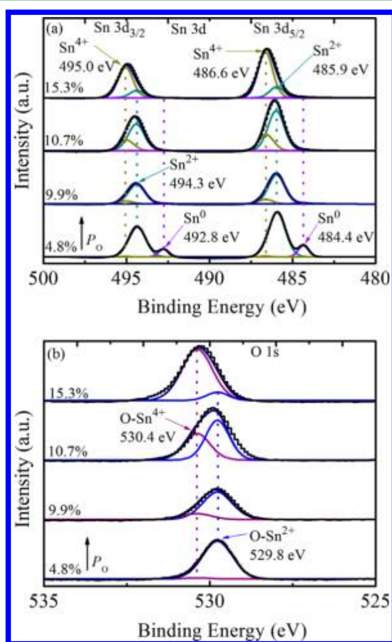


Figure 4. XPS spectra of (a) Sn 3d and (b) O 1s for the $SnO_x$ films under various oxygen partial pressure ($P_O$). Step lines and smooth lines are representing raw data and fitting data, respectively.

The contents of $SnO_2$, SnO, and Sn in the $SnO_x$ films were respectively calculated and illustrated in Figure 5. As $P_O$ increased to 6.5%, the Sn content decreased from ~14% to 0 nearly, whereas the SnO content increased to a maximum value (~96%), in a good agreement with the XRD observation that the $\beta$-Sn phase faded away and the $\alpha$-SnO-related peaks stretched out significantly. After that, the SnO content dropped persistently, approaching ~18% at $P_O$ = 15.3%, whereas the $SnO_2$ content increased from 0 till ~82% with $P_O$. Moreover, it was noted that, a crystallization transition from polycrystalline to amorphous was confirmed by XRD technique at $P_O$ = 10.7%, at which the $SnO_2$ content was ~27%. In other words, although having considerably high crystallization temperature (> 400°C).[27] $SnO_2$ was not the dominant phase at $P_O$ = 10.7% so that itself could not account for the crystallization transition exclusively. It is suggested that the involvement of $Sn^{4+}$ boosted the structural disorder in the $SnO_x$ matrix since $Sn^{4+}$−O and $Sn^{2+}$−O bonds have distinct coordination number, bond angle, and bond length, and so on, consequently improving the crystallization temperature.

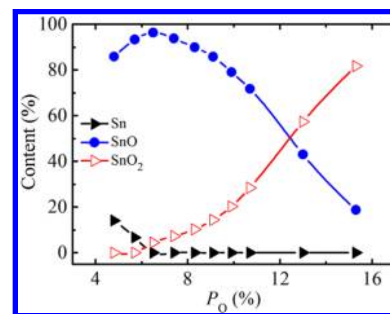


Figure 5. Content evolution of $SnO_2$, SnO, and Sn in the films as a function of oxygen partial pressure ($P_O$).

**Optical Properties.** Optical constants were obtained by fitting the SE data in the wavelength range of 300−1700 nm. Tauc-Lorentz dispersion function was employed to generate the refractive index $n$ and extinction coefficient $\kappa$ of the transparent films.[32] For films deposited at low $P_O$ with low transmittance, effective medium approximate (EMA) layer model with the intervention of metal tin layer was used to generate the optical constants. The EMA approach, as a very robust approach to describe the electromagnetic response of the heterogeneous system when the feature size of the nonuniform composition is smaller than the wavelength, is based on the Lorentz cavity concept for the determination of the polarizability of an individual inclusion and Clausius-Mossotti relation.[33]

Figure 6a presents the refractive index of the films with $P_O$. For clarity, the refractive index at 550 nm was selected and plotted in the inset of Figure 6a. At $P_O$ = 4.8%, the films with $\beta$-Sn and $\alpha$-SnO phases involved showed a lower refractive index than $\alpha$-SnO dominated films in the short wavelength range (<400 nm), simply owing to the smaller refractive index of $\beta$-Sn (0.37−1.0) in such range.[34] Whereas the refractive index of $\beta$-Sn increases dramatically with wavelength, for example, approaching ~3.15 at 930 nm.[34] Thus the films incorporated with $\beta$-Sn phase presented higher refractive index in the long wavelength range (greater than ~500 nm). With increasing $P_O$, however, the refractive index of the films decreased gradually, which was attributed to the increasing content evolution of $SnO_2$.[12] As reported, $SnO_2$ has a smaller refractive index (1.7−2.0 at 550 nm) than SnO (2.5−2.8 at 550 nm).[32,35,36] As expected in our experiment, the SnO-dominated films ($P_O \leq$ 9.9%) exhibited a refractive index (2.3−3.0 at 550 nm) higher than the $SnO_2$-dominated ($P_O \geq 12.3\%$) films (1.8−2.0 at 550 nm).

Optical band gaps $E_{gap}$ of the films were obtained on the basis of a graphical method (as shown in Figure 6b) using the following equation

$$(\alpha h\nu)^2 = A(h\nu - E_{gap}) \quad (2)$$

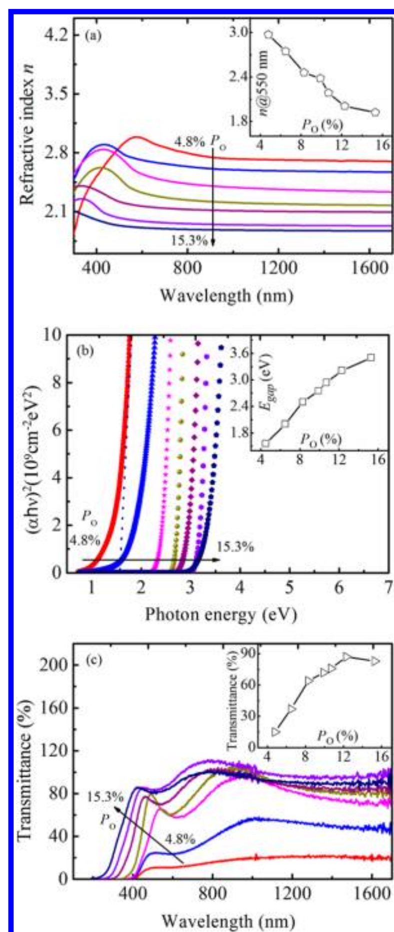


Figure 6. (a) Refractive index of the $SnO_x$ films under different oxygen partial pressure ($P_O$) as a function of wavelength. Inset is the refractive index at wavelength 550 nm vs. oxygen partial pressure. (b) $(\alpha h\nu)^2$ as a function of photon energy $h\nu$. Inset is the calculated band gap vs. oxygen partial pressure. (c) The transmittance spectra of the $SnO_x$ films with different oxygen partial pressure ($P_O$). Inset shows the average transmittance of the films.

where $\alpha$ is the absorption coefficient calculated via $\alpha = 4\pi\kappa/\lambda$ ($\lambda$ is the wavelength of incident light), and $A$ is a constant. The films at low $P_O$ have a very narrow band gap (1.5−2.0 eV), because $\beta$-Sn phase, acting as metallic particles or clusters, absorbs the light intensively. As $P_O$ increased, the $E_{gap}$ values of the films increased almost linearly (as presented in the inset of Figure 6b) from 2.0 to 3.5 eV because there is more $SnO_2$ available, because $SnO_2$ (3.6 eV) has a broader band gap than SnO (2.5−2.8 eV).[28]

Figure 6c shows the transmittance spectra of the films measured by SE at different $P_O$. As expected, the films with $\beta$-Sn phase included displayed a low transmittance in the whole spectra because of the intensive light absorption of the metal ingredient. The films without $\beta$-Sn phase incorporated illustrated a marginal difference in the transmittance at long wavelength (>800 nm), whereas the band edge shifted gradually to the shorter wavelengths as $P_O$ increased, which was consistent with the blue-shift of the band gaps. Hence, the average transmittance first increased rapidly and then tended to be saturated around 87% as $P_O$ varied (as shown in the inset of Figure 6c).

**Electrical Performances.** Figure 7 manifests the dependence of resistivity, Hall mobility and carrier concentration on

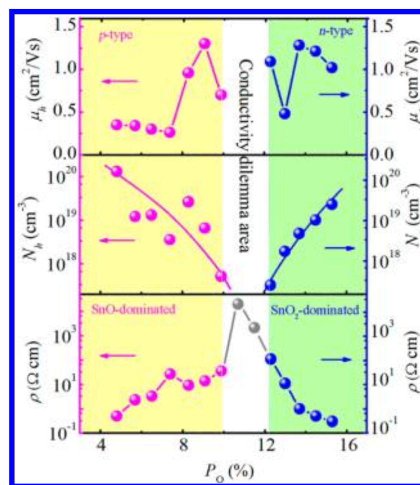


Figure 7. Resistivity $\rho$, hole/electron concentration $N_h/N_e$, and hole/electron mobility $\mu_h/\mu_e$ vs. oxygen partial pressure ($P_O$).

different $P_O$. The SnO-dominated films ($P_O \leq 9.9\%$) exhibited p-type conduction behavior with the mobility, the hole concentration, and the resistivity in the range of 0.3−1.3 cm$^2$/(V s), $1 \times 10^{17}$ to $1 \times 10^{20}$ cm$^{-3}$, and 0.5−35 Ω cm, respectively. Generally speaking, the hole concentration displayed a decreasing trend with increasing $P_O$ in the range of 4.8−9.9%. On the basis of first-principle calculations, the p-type conductivity of SnO films originates from the excess of oxygen or/and the tin vacancy ($V_{Sn}$);[37] meanwhile, experimental results also confirmed that a SnO film with a high O/Sn ratio favors the formation of acceptors $V_{Sn}$, which thus produces more mobile holes.[38] However, this suggestion can not interpret the decreasing trend of the hole concentration in the SnO-dominated films, instead a carrier compensation effect is believed to account for that. According to the XPS results, a certain amount of $Sn^{4+}$ ions were involved into the SnO-dominated films yet, and the $Sn^{4+}$ content increased persistently with $P_O$. It is speculated that, the $Sn^{4+}$ ion and/or its relate defect state acting as donors or hole killers, would compensate and/or capture a portion of free holes generated in the SnO-dominated films, consequently the hole concentration dropped with increasing $P_O$. When the number of free electrons has approximately the same order of magnitude with the free holes, the $SnO_x$ films would display the maximum resistivity, which were observed for the films at $P_O$ around 10.7% as named "conductivity dilemma area". The carrier concentration and mobility of the films fabricated at $P_O$ = 10.7% and 11.5% were not available because of their high resistivity (~$1 \times 10^4$ Ω cm), which is beyond the capability of the Hall-effect measurement. As $P_O$ kept increasing, a conductivity inversion from p- to n-type was observed. For example, when $P_O$ ranged from 12.3 to 15.3%, the $SnO_2$-dominated films demonstrated n-type conduction behavior unambiguously with a mobility in the range of 0.5−1.3 cm$^2$/(V s), an increasing electron concentration ranging from $1 \times 10^{17}$ to $1 \times 10^{19}$ cm$^{-3}$, and a decreasing resistivity from 108 to 0.3 Ω cm, respectively.

## CONCLUSION

$SnO_x$ films were fabricated by reactive rf magnetron sputtering followed by a low temperature annealing at 200 °C, and the influence of oxygen partial pressure ($P_O$) on the various properties of the films was systematically investigated. It can be roughly divided into three $P_O$ regions to describe the structural

and electrical evolution of the films: (1) $P_O \leq 9.9\%$, the films presented a p-type conduction, in which polycrystalline SnO phase dominated. (2) $9.9\% < P_O < 12.3\%$, the films exhibited a characteristic of "conductivity dilemma area", where the crystallization temperature was improved so that a transition from polycrystalline to amorphous occurred, because the involvement of $Sn^{4+}$ augmented the structural disorder in the $SnO_x$ matrix. (3) $P_O \geq 12.3\%$, the films displayed an n-type behavior with increasing electron concentration as $P_O$ increased, in which amorphous $SnO_2$ phase took the privileges. Moreover, the optical parameters presented a monotonic variation with increasing $P_O$, i.e., the refractive index decreased from 3.0 to 1.8 and the band gap increased from 1.5 to 3.5 eV, because of increasing content evolution of $SnO_2$. These results supply a comprehensive investigation on the structural, chemical, optical, and electrical property evolutions for the community of tin oxides, which would offer an opportunity to boost their further exploration and development.

## AUTHOR INFORMATION

### Corresponding Author

*E-mail: h_cao@nimte.ac.cn (H.T.C.); lly@nimte.ac.cn (L.Y.L.).

### Notes

The authors declare no competing financial interest.

## ACKNOWLEDGMENTS

This work is supported by the Chinese National Program on Key Basic Research Project (2012CB933003), the National Natural Science Foundation of China (Grants 11104289 and 61274095), the Science and Technology Innovative Research Team of Ningbo Municipality (2009B21005), the Key Program for Science and Technology Innovative Team of Zhejiang Province (2010R50020), and Applied Research Funds for Public Welfare Project of Zhejiang Provience (2011C21030).

## REFERENCES

(1) He, Y. S.; Campbell, J. C.; Murphy, R. C.; Arendt, M. F.; Swinnea, J. S. *J. Mater. Res.* **1993**, *8*, 3131−3134.
(2) Presley, R. E.; Munsee, C. L.; Park, C. H.; Hong, D.; Wager, J. F.; Keszler, D. A. *J. Phys. D* **2004**, *37*, 2810−2813.
(3) Ferrere, S.; Zaban, A.; Gsegg, B. A. *J. Phys. Chem. B* **1997**, *101*, 4490−4493.
(4) Leite, E. R.; Weber, I. T.; Longo, E.; Varela, J. A. *Adv. Mater.* **2000**, *12*, 965−968.
(5) Calderer, J.; Molinas, P.; Sueiras, J.; Llobet, E.; Vilanova, X.; Correig, X.; Masana, F.; Rodriguez, A. *Microelectron. Reliab.* **2000**, *40*, 807−810.
(6) Watson, J. *Sens. Actuators.* **1984**, *5*, 29−42.
(7) Odani, A.; Nimberger, A.; Markovsky, B.; Sominski, E.; Levi, E.; Kumar, V. G.; Motiei, M.; Gedanken, A.; Dan, P.; Aurbach, D. *J. Power Sources* **2003**, *119*, 517−521.
(8) Aurbach, D.; Nimberger, A.; Markovsky, B.; Levi, E.; Sominski, E.; Gedanken, A. *Chem. Mater.* **2002**, *14*, 4155−4163.
(9) Uchiyama, H.; Hosono, E.; Honma, I.; Zhou, H. S.; Imai, H. *Electrochem. Commun.* **2008**, *10*, 52−55.
(10) Pan, X. Q.; Fu, L. *J. Appl. Phys.* **2002**, *89*, 6048−6055.
(11) Fortunato, E.; Barros, R.; Barquinha, P.; Figueiredo, V.; Park, S. H. K.; Hwang, C. S.; Martins, R. *Appl. Phys. Lett.* **2010**, *97* (052105), 1−3.
(12) Liang, L. Y.; Liu, Z. M.; Cao, H. T.; Yu, Z.; Shi, Y. Y.; Chen, A. H.; Zhang, H. Z.; Fang, Y. Q.; Xi Lian Sun, X. L. *J. Electrochem. Soc.* **2010**, *157*, H598−H602.
(13) Ogo, Y.; Hiramatsu, H.; Nomura, K.; Yanagi, H.; Kamiya, T.; Hirano, M.; Hosono, H. *Appl. Phys. Lett.* **2008**, *93* (032113), 1−3.
(14) Martins, R.; Nathan, A.; Barros, R.; Pereira, L.; Barquinha, P.; Correia, N.; Costa, R.; Ahnood, A.; Ferreira, I.; Fortunato, E. *Adv. Mater.* **2011**, *23*, 4491−4496.
(15) Nomura, K.; Kamiya, T.; Hosono, H. *Adv. Mater.* **2011**, *23*, 3431−3434.
(16) Liang, L. Y.; Cao, H. T.; Chen, X. B.; Liu, Z. M.; Zhuge, F.; Luo, H.; Li, J.; Lu, Y. C.; Lu, W. *Appl. Phys. Lett.* **2012**, *100* (263502), 1−5.
(17) Kumar, B.; Lee, D. H.; Kim, S. H.; Yang, B.; Maeng, S.; Kim, S. W. *J. Phys. Chem. C.* **2010**, *114*, 11050−11055.
(18) Sakaushi, K.; Oaki, K.; Uchiyama, H.; Hosono, E.; Zhou, H. S.; Imai, H. *Small* **2010**, *6*, 776−781.
(19) Zubair Iqbal, M.; Wang, F. P.; Rafi, U. D.; Javed, Q. U. A.; Yasir Rafique, M.; Li, Y.; Li, P. F. *Mater. Lett.* **2012**, *68*, 409−412.
(20) Muranaka, S.; Bando, Y.; Takada, T. *Thin Solid Films* **1981**, *86*, 11−19.
(21) Beensh Marchwicka, G.; Stepniewska, L. K.; Misiuk, A. *Thin Solid Films* **1984**, *113*, 215−224.
(22) Olijnyk, H. *Phys. Rev. B* **1992**, *46*, 6589−6591.
(23) Lewis, S. P.; Cohen, M. L. *Phys. Rev. B* **1993**, *48*, 3646−3653.
(24) Peltzer y Blanca, E. L.; Svane, A.; Christensen, N. E.; Rodriguez, C. O.; Cappannini, O. M.; Moreno, M. S. *Phys. Rev. B* **1993**, *48*, 15712−15718.
(25) Sun, S. H.; Meng, G. W.; Zhang, G. X.; Gao, T.; Geng, B. Y.; Zhang, L. D.; Zuo, J. *Chem. Phys. Lett.* **2003**, *376*, 103−107.
(26) Chen, Z. W.; Lai, J. K. L.; Shek, C. H. *Phys. Rev. B* **2004**, *70* (165314), 1−7.
(27) Zenkyu, R.; Tauima, D.; Yuhara, J. *J. Appl. Phys.* **2012**, *111* (064907), 1−6.
(28) Geurts, J.; Rau, S.; Richter, W.; Schmitte, F. J. *Thin Solid Films* **1984**, *12*, 217−225.
(29) Koval, K.; Burriel, R.; Stachiotti, M. G.; Castro, M.; Migoni, R. L.; Moreno, M. S.; Varela, A.; Rodriguez, C. O. *Phys. Rev. B* **1999**, *60*, 14496−14499.
(30) Szuber, J.; Czempik, G.; Larciprete, R.; Koziej, D.; Adamowicz, B. *Thin Solid Films* **2001**, *391*, 198−203.
(31) Her, Y. C.; Wu, J. Y.; Lin, Y. R.; Tsai, S. Y. *Appl. Phys. Lett.* **2006**, *89* (043115), 1−3.
(32) Liang, L. Y.; Liu, Z. M.; Cao, H. T.; Shi, Y. Y.; Sun, X. L.; Yu, Z.; Chen, A. H.; Zhang, H. Z.; Fang, Y. Q. *ACS Appl Mater. Interfaces* **2010**, *2*, 1565−1568.
(33) Aspnes, D. E. *Am. J. Phys.* **1982**, *50*, 704−709.
(34) Palik, E. D. *Handbook of Optical Constants*; Academic Press: San Diego, 1998; Vol. 3, pp 271−274.
(35) Paulson, P. D.; Hegedus, S. S. *J. Appl. Phys.* **2004**, *96*, 5469−5477.
(36) Kim, T. W.; Lee, D. U.; Choo, D. C.; Kim, J. H.; Kim, H. J.; Jeong, J. H.; Jung, M.; Bahang, J. H.; Park, H. L.; Yoon, Y. S.; Kim, J. Y. *J. Phys. Chem. Solids* **2002**, *63*, 881−885.
(37) Togo, A.; Oba, F.; Tanaka, I.; Tatsumi, K. *Phys. Rev. B* **2006**, *74* (195128), 1−8.
(38) Guo, W.; Fu, L.; Zhang, Y.; Zhang, K.; Liang, L. Y.; Liu, Z. M.; Cao, H. T.; Pan, X. Q. *Appl. Phys. Lett.* **2010**, *96* (042113), 1−3.

## NOTE ADDED AFTER ASAP PUBLICATION

This paper was published on the Web on October 11, with errors in the Synopsis and Abstract graphic. The corrected version was reposted on October 15, 2012.